MSDE

Molecular Systems Design & Engineering

Accepted Manuscript

This article can be cited before page numbers have been issued, to do this please use: M. S. Pacella, V. Mardanlou, S. Agarwal, A. Patel, E. Jelezniakov, A. M. Mohammed, E. Franco and R. Schulman, *Mol. Syst. Des. Eng.*, 2019, DOI: 10.1039/C9ME00068B.

ROYAL SOCIETY OF CHEMISTRY

rsc.li/molecular-engineering

View Article Online
DOI: 10.1039/C9ME00068B

Design, System, Application

The DNA nanotubes described in our paper are molecularly designed to self-assemble from monomeric DNA tiles and to undergo polymer end-to-end joining processes. The nucleation and growth of our DNA nanotubes is controlled via DNA origami seeds that can be attached to various landmarks. Their primary functionality is to connect molecular landmarks, be they on a single solid surface, two parallel surfaces, or on two separate particles. The important design constraints to consider are (a) the persistence length of the nanotubes, (b) the average length of the nanotubes, (c) the rate of end-to-end joining of the nanotubes, (d) the concentration of monomeric DNA tiles that form the nanotubes, (e) the concentration of the DNA origami seeds that nucleate the nanotubes. In the future, we hope that our nanotubes may be used to synthetically reproduce the functionality of the cellular cytoskeleton by forming designable networks that can be controllably reconfigured.

Characterizing the Length-Dependence of DNA Nanotube End-to-End Joining Rates

View Article Online
DOI: 10.1039/C9ME00068B

dReceived 00th January 20xx,
Accepted 00th January 20xx

DOI: 10.1039/x0xx00000x

www.rsc.org/

Michael S. Pacella,[a] Vahid Mardanlou,[b] Siddharth Agarwal,[b] Anusha Patel,[a] Elizabeth Jelezniakov,[c] Abdul M. Mohammed,[d] Elisa Franco,[b] and Rebecca Schulman[a,e]

DNA nanotechnology offers a route towards the synthesis of custom nano-structured materials and circuits through hierarchical assembly processes. While predictive kinetic models are being developed for the assembly of DNA nanostructures from small monomeric components, a general model for the hierarchical assembly of DNA nanostrutures remains elusive. DNA tile nanotubes provide an ideal model system for the study of hierarchical assembly *via* end-to-end joining. In this study, we experimentally characterize the length-dependence of the end-to-end joining rate of DNA tile nanotubes. We then test the ability of three different models of polymer end-to-end joining to reproduce experimentally measured changes in nanotube lengths during a joining reaction using an ODE model for nanotube joining. All three models predict physically realistic joining rates that are consistent with prior measurements, with a length-independent end-to-end joining rate model providing the best fit to the experimental data. A length-independent constant joining rate is consistent with other DNA self-assembly processes across a broad range of length scales and also suggests how tractable models for hierarchical DNA nanostructure could be developed. .

Introduction

A longstanding goal of nanotechnology is the development of methods for synthesizing custom matter from the ground up in a hierarchical fashion. As described by Drexler,[1] an 'atomic assembler' is a device that can build materials atom-by-atom to yield any specified design pattern. DNA nanotechnology offers a route towards the synthesis of custom nano-structured materials and circuits through controlled self-assembly processes,[2-4] although of DNA oligonucleotides rather than atoms. Self-assembly in particular offers not only the ability to inexpensively assemble structures with very small features, but also the ability to create materials that are capable of autonomous reconfiguration in response to stimuli.[5-9]

An essential challenge is the self-assembly of designed structures with feature sizes ranging from nanometers to tens of microns or beyond.[10-17] At very large size scales, hierarchical self-assembly, which allows molecules to assemble to form a desired structure in parallel, is likely to be important for efficient self-assembly. An understanding of the kinetics of hierarchical self-assembly processes and the development of models and design tools will therefore enable the development of reliable fabrication processes for complex structures and custom materials.[18-21] One challenge in hierarchical self-assembly is that interactions may occur between objects of very different sizes. Because structure size affects diffusion rates and the ability of reactants to properly orient, understanding how structure size affect rates of binding will be crucial for the accurate determination of assembly reaction rates. In this work, we investigate the kinetics of micron-scale DNA nanostructure assembly using a model system: we characterize the length-dependence of DNA tile nanotube joining rates. We experimentally measure changes in the distribution of nanotube lengths due to end-to-end joining and test the ability of three models of end-to-end joining rates (two length-dependent, one length-independent) to reproduce the experimental length data.

DNA nanostructures exploit programmable Watson-Crick base pairing interactions between DNA molecules to achieve a specific final shape. In the folding of scaffolded DNA origami[22] for example, a single ~7,000 base 'scaffold' strand is used as a template to organize hundreds of shorter 'staple' strands. The staple strands hybridize with multiple regions of the scaffold strand, generally at points separated by hundreds or more bases. This assembly process forces the template into a compact folded structure that for typical scaffold lengths is tens of nanometers in size.[20, 23] The driving force for origami folding is hybridization of complementary regions of single stranded DNA.[23] In addition to folded DNA origami, smaller nanostructures such as DNA tiles[21, 24-26] can also be assembled via base pair complementarity. These tiles as well as DNA origami structures can each self-assemble into hierarchical structures such as 2-D and 3-D lattices that may grow to the micrometer scale.[27] At this scale, a combination of DNA hybridization, shape complementarity between DNA origamis as well as blunt end helix stacking is used to drive assembly.[20] Further assembly to form structures with even larger sizes may require further steps of hierarchical assembly.[28]

While predictive kinetic models exist for the assembly of some DNA nanostructures (e.g. DNA nanotubes) from small monomeric components (e.g. DNA tiles),[29] a general model for the hierarchical assembly of DNA nanostructure assemblies from larger components (e.g. long DNA nanotubes from short DNA nanotubes) remains elusive.[16, 18, 30] Such a model could enable the programming of more rapid, higher yield hierarchical self-assembly or material reconfiguration processes.

DNA nanotubes and other one-dimensional self-assembling filaments are good models for the understanding of general principles of self-assembly. DNA nanotubes have been

[a] *Chemical and Biomolecular Engineering, Johns Hopkins University, Baltimore, Maryland 21218, United States.*
[b] *Mechanical Engineering, University of California at Riverside, California 92521, United States.*
[c] *Baltimore Polytechnic Institute, Baltimore, Maryland 21209, United States.*
[d] *Ultivue, Cambridge, Massachusetts 02138, United States.*
[e] *Computer Science, Johns Hopkins University, Baltimore, Maryland 21218, United States.*

† Footnotes relating to the title and/or authors should appear here.
Electronic Supplementary Information (ESI) available: [details of any supplementary information available should be included here]. See DOI: 10.1039/x0xx00000x

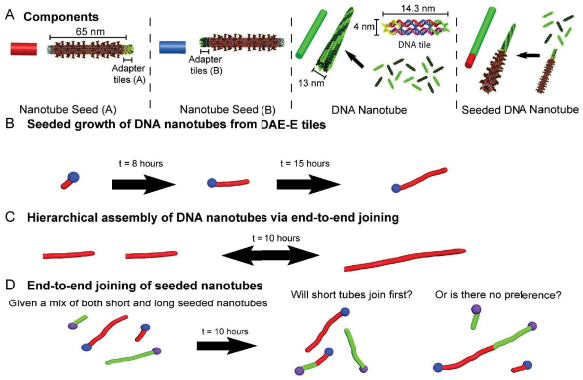

Figure 1. Overview of DNA nanotube growth and end-to-end joining. (A) DNA origami seeds and DNA nanotubes composed of DNA tiles. (B) seeded growth of DNA nanotubes. (C) End-to-end joining of two unseeded nanotubes. (D) End-to-end joining of seeded nanotubes.

assembled using a range of structural motifs. In this paper, we study the joining rates of DAE-E tile DNA nanotubes, linear polymers composed of monomeric DNA crossover tiles that assemble into cylindrical tubes as a result of single-stranded "sticky end" hybridization between adjacent tiles.[31] (Figure 1). The structure, stiffness, growth, nucleation and diffusion rates of these nanotubes have been studied previously under a range of conditions.[18, 29, 31-33] These structures have a persistence length of 8.7+/-.5 μM, making nanotubes of lengths of 1-20 μM semiflexible. Their rotational and translational diffusion in standard buffers follows classic scaling laws for polymer diffusion.[18]

DNA nanotube joining represents a special case of the broader problem of polymer joining. The simplest case of the polymer joining problem is the end-to-end association of two freely mobile rigid rods in solution. A theoretical analysis by Hill[34], based on diffusional arguments presented by Riseman and Kirkwood,[35] suggests that the bimolecular association rate constant β for two rigid rods of lengths N_1 and N_2 diffusing freely in solution should follow the form

Equation 1

$$\beta_{N_1N_2} \sim A_{Hill}(N_2 ln N_1 + N_1 ln N_2)/N_1N_2N$$

where A_{Hill} is a length-independent prefactor and $N = N_1 + N_2$. Under this form, the joining rate is symmetric about $N_1 = N_2$ and reaches a minimum value at $N_1 = N_2$ for a fixed total length of the reactants $N = N_1 + N_2$.

Another theoretical treatment of the end-to-end association of two freely mobile rigid rods is provided by Hariadi *et al.*[32] Similar to Hill, the authors invoke the same arguments from Riseman and Kirkwood[35] to derive length-dependent translational diffusion constants for each rod. However, while Hill enforces the condition that the two rods must be approximately aligned in order to successfully join, Hariadi *et al.* assume that the reactive ends of the rods can initiate successful joining regardless of their orientation. The resulting expression for the bimolecular association rate constant β for two rigid rods of lengths N_1 and N_2 diffusing freely in solution is

Equation 2

$$\beta_{N_1N_2} \sim A_{Hariadi}\kappa(N_2 ln N_1 + N_1 ln N_2)/N_1N_2$$

View Article Online
DOI: 10.1039/C9ME00068B

where $A_{Hariadi}$ is a length-independent prefactor and κ is an effectiveness parameter that determines the probability that a joining event occurs each time the rod ends meet.

Experimental studies of rigid rod end-to-end joining have focused mainly on microtubules,[36-39] amyloid fibrils,[40-42] and actin filaments.[43, 44] In studies by Williams and Rone,[38, 39] taxol was used to stabilize microtubules so that the end-to-end joining rate could be measured independently of tubulin subunit exchange. The authors observed that the association rate decreases with increasing microtubule length, in agreement with Hill's model. However, they observed less than second order kinetics, implying that molecular crowding plays a role at higher microtubule concentrations. Bachand *et al.*[36] and Greene *et al.*[37] used fluorescence microscopy to measure the rate of assembly of microtubule nano-arrays from sheared microtubule filaments. The use of fluorescent labels allowed the authors to track microtubules that had undergone end-to-end joining and distinguish them from microtubules that had not undergone joining, yielding results that show diffusion-limited second order kinetics in agreement with Hill's model. Using a synthetic β-amyloid peptide, Tomski and Murphy[42] observed diffusion limited aggregation also in agreement with Hill's model. Annealing sheared actin tropomyosin filaments, Teubner and Wegner[43] also observed a length-dependent end-to-end joining rate in agreement with Hill.

Because the sticky ends on one side of the tile are complementary to the sticky ends on the opposite side, DNA nanotubes, like microtubules, have an inherent directionality. The persistence length of DNA nanotubes (~10 μm) is roughly three orders of magnitude less than the persistence length of a microtubule (~5000 μm), casting doubt on the validity of the rigid rod model for nanotube end-to-end joining on a scale of tens of microns.

A range of previous studies support end-to-end joining as a major factor in the assembly of DAE-E tile nanotubes and related structures under a range of assembly conditions. Ekani-Nkodo *et al.*[31] observed nanotube end-to-end joining directly using optical microscopy with fluorescently labelled DAE-E DNA tiles and determined that under the high supersaturation conditions considered, end-to-end joining, not Ostwald ripening, was responsible for the decrease in the number of observed nanotubes over time. Mohammed *et al.*[18] studied the

end-to-end joining of DNA nanotubes nucleated from DNA origami seeds. Utilizing optical microscopy and fluorescent labelling of both the origami seed and the DNA nanotubes, Mohammed *et al.* were able to measure nanotube joining rates and compare the results against a coarse-grained worm-like chain model of nanotube dynamics and joining. Hariadi *et al.*[32] used a model of DNA nanotube fragmentation (and subsequent joining) to study the strength of fluid flows within bursting bubbles.

These previous observations of DNA nanotube joining did not investigate the length-dependence of the joining rate. In the kinetic models developed for these systems, the nanotube joining rate is either length-independent, or (in the Hariadi *et al.* study) assumes a specific length-dependence that is never independently validated. The goal of our work is to experimentally characterize the length dependence of DNA nanotube joining rates and assess the accuracy of current models of nanotube joining.

We measure the joining rate of DNA nanotubes by separately growing two populations of seeded nanotubes (each with a unique fluorescent label). Once polymerization and depolymerisation have reached an equilibrium (nanotubes stop growing), we mix the populations and periodically place a sample of the mixed populations on a glass slide to look at the structure of the nanotubes within the mixture. We use fluorescence microscopy to determine the extent of joining and the lengths of the joined tubes at different time points (Figure 2). We use the length distributions of both joined and unjoined nanotubes at each time point to determine if there is a length dependence on the joining rate.

Two types of seeds, denoted "A" and "B", are employed in this study (see Mohammed *et al.*[29] for details regarding seed design and structure). The two seeds respectively nucleate growth in each of the two possible directions. The direction of growth off of a seed is controlled by the sequence of adapter strands that present sticky end sequences for tile binding. Because the sticky ends exposed at the two types of nanotube ends are complementary, nanotubes may end-to-end join with one another *via* Watson-Crick base pairing. However, nanotubes seeded from A seeds cannot join to one another because they all present the same type of ends. Likewise, nanotubes seeded from B seeds cannot join to other B-seeded nanotubes. Henceforth, we will use the labels "A" and "B" to distinguish these two populations of seeds and seeded nanotubes. Additionally, we will use the label "C" to refer to nanotubes that have end-to-end joined and contain both an A and a B seed.

We first grew A and B seeded nanotubes in separate solutions and waited ~15 hours until nanotube growth had stagnated, as indicated by mean nanotube length reaching a plateau. At this point both A and B solutions contained seeded nanotubes with a distribution of lengths. We then mixed the A and B solutions together in a 1:5 ratio. Including the B species in 5-fold excess to the A species means that the distribution of lengths of B seeded nanotubes should not be affected significantly by the end-to-end joining process, allowing us to measure joining by looking at changes in the lengths of the A seeded nanotubes over time. Distinct fluorescent labels for

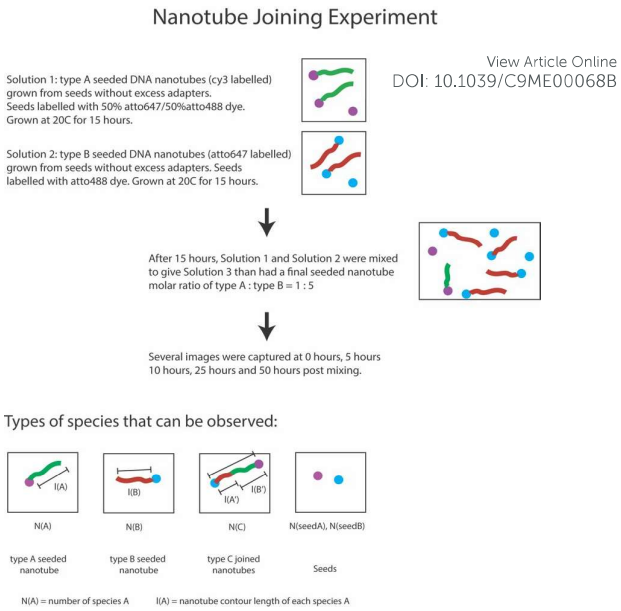

Figure 2. Overview of experimental protocol used to observe nanotube end-to-end joining.

both A and B seeds and tubes (see Methods) allowed us to independently track the length distributions of A and B seeded nanotubes using fluorescence microscopy as well as to identify nanotubes that have undergone end-to-end joining (C nanotubes) and measure both their total lengths and the lengths of both the A and B components of the joined tube. By comparing the distributions of nanotube lengths during these experiments to the distributions of lengths predicted by different joining models we could determine which models of joining are consistent with DNA nanotube joining in experiments.

Methods

Nanotube Joining Experiments

DNA Nanotube and Seed Assembly Mixtures. We grew seeded DNA nanotubes following the protocol outlined by Mohammed.[18] Tile, adapter, and seed strand sequences used in this study are listed in Supporting Information. DNA tile, adapter, and staple strands were synthesized by Integrated DNA Technologies, Inc. Adapter and tile strands were PAGE purified. "A" seeds were labelled using 50% atto488 fluorescent dye and 50% atto647 fluorescent dye allowing fluorescence imaging of the seed. To distinguish "B" seeds from "A" seeds, "B" seeds were labelled using 100% atto488 fluorescent dye. DNA nanotubes nucleated from "A" seeds were labelled with cy3 dye and nanotubes nucleated from "B" seeds were labelled with atto647. All samples were prepared in TAE buffer (40 mM tris-Acetate, 1mM EDTA) to which 12.5 mM magnesium acetate was added. In the initial A solution, the strands for each tile were present at 55 nM except for the strands presenting sticky ends, which were present at 110 nM to minimize the concentration of malformed tiles. In the initial B solution, the

strands for each tile were present at 175 nM (sticky end strands at 350 nM.) Both A and B DNA origami seeds were prepared as described in Agrawal *et al.*,[45] with the only differences between A and B seeds being the sequences of the adapter strands and the identities of the fluorophore used to label them.

Nanotube Annealing. Samples were annealed using an Eppendorf Mastercycler in a two-pot reaction. In one pot, DNA tiles were annealed from 90 °C to 20 °C at 1 °C/min. In a second pot, DNA origami seeds were annealed using the protocol described by Agrawal *et al.* After annealing, the seeds were purified using centrifugal filtration to remove excess staples and adapters not incorporated into seeds (as described in Agrawal *et al.*[45]) Purified seeds were then added to the annealed tiles at a concentration of approximately 6 pM and incubated at 20 °C for 15 hours. "A" solution and "B" solution samples were prepared separately during this process. After separately incubating the A and B solutions for 15 hours, the solutions were combined in a 1:5 A:B ratio and incubation was continued at 20 °C.

Fluorescence Microscopy. After combining the A and B solutions, fluorescence microscopy images were taken at 0.5 hr, 2.5 hr, and 4.5 hr post mixing. 6 µL of the combined A/B solution was transferred to an 18 mm by 18 mm glass coverslip for fluorescence imaging. The samples were imaged on an inverted microscope (Olympus IX71) using a 60x/1.45 NA oil immersion objective using an Olympus cy3 filter cube set (Z532BP). Images were captured on a cooled CCD camera (iXon3, Andor).

Nanotube Image Processing. Fluorescence microscopy images of nanotubes were processed in an automated fashion using the scikit-image[46] library available for Python. First, edge detection was performed using the Canny algorithm.[47] Small gaps in the detected edges were closed by applying a dilation (to join adjacent edges) followed by an erosion (to restore a single pixel-width edge). Closed tubes were then filled using mathematical morphology. Finally, artifacts were removed by applying a filter to remove detected objects below a threshold size and eccentricity. Because we expect nanotubes to be of a consistent width, nanotube length (in pixels) was calculated by dividing the total number of pixels in a tube by the mean width of the tubes in a given image. The length in pixels was then multiplied by .17 µm/pixel to calculate the final length in microns. This process was used to independently detect nanotubes present in the cy3 channel and the atto647 channel for each image. Nanotube ends were then detected by using skeletonization[48] to reduce each tube to a 1 pixel wide representation and then searching the image for pixels with only a single neighbour. These pixels were assumed to be the tube endpoints. A nanotube was then defined as "joined" if one of its endpoints was within a cutoff distance of another nanotube endpoint present in the alternative channel (*i.e.* a cy3 nanotube endpoint in proximity to an atto647 nanotube endpoint). A Python script to perform the described nanotube image processing is available upon request.

Kinetic Model of Nanotube Joining

We model the evolution of length distributions in a DNA nanotube population where two distinct subpopulations, grown from different types of DNA origami seeds, join to form hybrid nanotubes. The goal of the model is to obtain an estimate for the joining rate of the subpopulations. We follow the approach of Mardanlou *et al.*, in which a deterministic, course-grained model is derived to take into account nanotube nucleation, polymerization, depolymerisation, and length-dependent nanotube joining.[49] To focus our analysis on nanotube joining, we designed our experiments so that the expected rates of tile nucleation and the net rate of polymerization and depolymerization are negligible, so that nucleation, polymerization and depolymerization processes can be ignored under the conditions of our experiment (see Results for experimental validation of this assumption). Fragmentation of nanotubes like those considered here proceeds at a negligible rate (Mardanlou *et al.*[50] and Fygenson *et al.*[31]), and thus is not included in the model.

The model captures temporal changes in the length distribution of the population of DNA nanotubes by tracking the concentrations of nanotubes of different lengths. The continuous length distribution is binned, and the evolution of the population of nanotubes in each length bin is modelled using ordinary differential equations derived from equivalent reactions.

Two nanotube "species" are present in our samples: A-type and B-type, which are designed to join. A joined A-B nanotube is classified as species C. Thus, we assume

$$A + B \xrightarrow{\beta} C,$$

where β is their joining rate.

Within our model, the population of each nanotube species is segmented by length: to obtain a computationally tractable model we choose a bin width of 1 µm, and we indicate the concentration of A-species nanotubes having length between 0 and 1 µm as [A1], those having length between 1 and 2 µm as [A2], and so on, with [An] indicating the concentration of nanotubes having length between (n-1) and n µm. A consistent notation choice is made for segments of the population of B nanotubes.

We then model all the possible combinations of interactions of nanotubes A and B in different length bins:

$$A1 + B1 \xrightarrow{\beta 11} C1,1$$
$$A1 + B2 \xrightarrow{\beta 12} C1,2$$
$$A1 + B3 \xrightarrow{\beta 13} C1,3 \ldots$$
$$Ai + Bj \xrightarrow{\beta ij} Ci,j$$

where Ci,j indicates C-type nanotubes that result from joining of A and B nanotubes that are respectively in the i µm and j µm length bin. These macroscopic chemical reactions are converted to ordinary differential equations (ODEs) using the law of mass action. Because we neglect nucleation and polymerization as well as fragmentation, the only terms present in the ODEs modelling the concentration of A and B nanotubes in each bin are those resulting from the joining reactions:

$$\frac{d[Ai]}{dt} = -[Ai]\sum_j \beta ij\ [Bj]$$
$$\frac{d[Bi]}{dt} = -[Bi]\sum_j \beta ij\ [Aj]$$

where i=1,…,i_{max} And j=1,…,j_{max} We decided on values of i_{max} and j_{max} of 10 based on the observed lengths of A and B type nanotubes. Although nanotubes longer than 10 µm were occasionally observed, they do not contribute significantly to the distribution of tube lengths and thus were not characterized. C type nanotubes are modelled by ODEs:

$$\frac{d[Ci,j]}{dt} = \beta ij[Bi][Aj]$$

The maximum length considered for a C type nanotube was $20\mu m$ (twice the maximum length of the A and B components). Given our choice of bin width, and the chosen threshold of maximum nanotube length, the model is composed of $20\times20 = 400$ independent ODEs.

In this study, we tested three possible expressions for nanotube joining rates: the length-dependent rate proposed by Hill et al. (Equation 1), the length-dependent rate proposed by Hariadi et al. (Equation 2) and a length-independent constant rate. Each joining rate expression contains exactly one adjustable parameter, which we fit to experimental data using brute force sampling. We assume that at t=0 only A and B type tubes are present and C type tubes have not yet formed. The concentrations of A and B type tubes at t=0 is derived from the experimental data by imaging the populations and counting the number of tubes of each population when they are mixed together. We assume that the actual density of nanotubes is double this count (half the nanotubes land on the imaging surface and other half of the non-imaging surface) (Mardanlou *et al.* in preparation, Agrawal *et al.*[45]). The final concentration of tubes in solution is the number of nanotubes divided by the volume of the sample observed microscopically and Avogadro's constant. We compare simulation results with experimental results at times t = .5, 2.5, and 4.5 hrs.

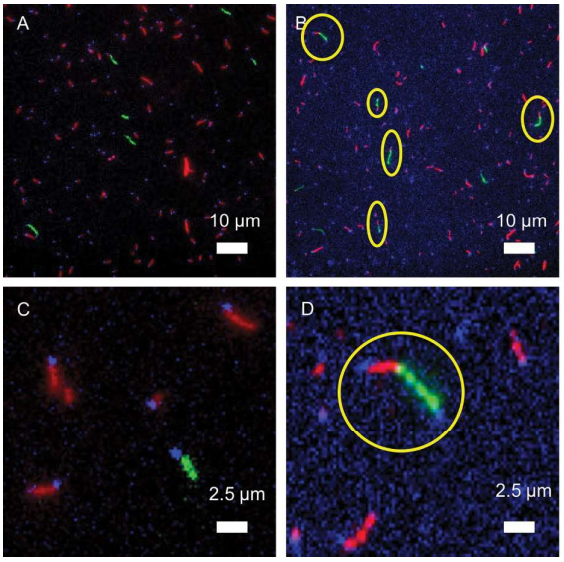

Figure 3. Fluorescence microscopy images of DNA nanotubes after end-to-end joining reactions lasting different periods of time. Red tubes are type-A (labelled with atto647), Green tubes are type-B (labelled with cy3). Purple dots are type A seeds (labelled with 50% atto647 and 50% atto488). Blue dots are type B seeds (labellwed with atto488). (A) .5 hrs post mixing (scale bar: 10µm). (B) 4.5 hrs post mixing (scale bar: 10µm). (C) Zoomed in view of A (scale bar 2.5 µm). (D) Zoomed in view of B (scale bar 2.5µm).

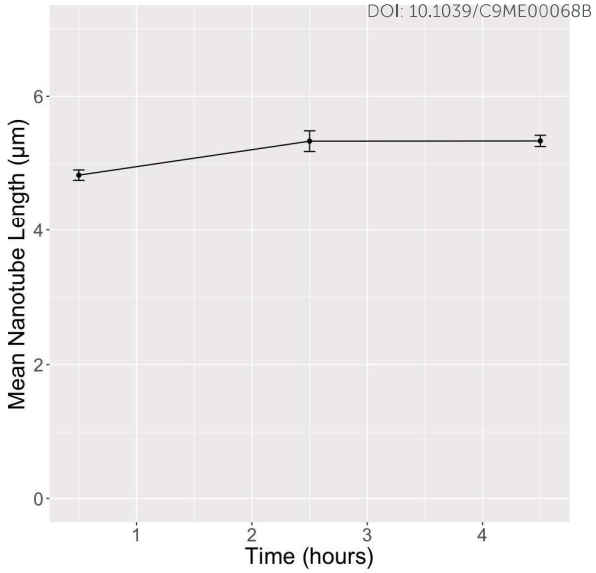

Figure 4. Mean lengths of seeded B-type nanotubes incubated in the absence of the A-type species (so that no end-to-end joining could occur). Error bars represent the standard error of the mean, calculated using bootstrapping with 1000 replicates.

Results

We collected 25 images at three time points (.5 hrs, 2.5 hrs, 4.5 hrs). For each image, we collected data from both the cy3 channel and the atto647 channel to obtain information about both the A and B nanotube species. Representative images of joined and unjoined nanotubes are shown in Figure 3. Using automated image processing (see Methods section), we measured the lengths of roughly 2000 nanotubes at each time point and assigned each tube a "joined" or "unjoined" status. When a joined A tube is identified by our algorithm, the B tube that it is joined with is also recorded and the lengths of the A and B components are summed to give the total length of the corresponding C type nanotube. Thus, for each time point we measured the length distributions of five species: unjoined A tubes, unjoined B tubes, joined A tubes, joined B tubes, and C tubes. We binned the lengths of each species using a 1 µm bin width and assuming a maximum tube length of 20 µm. Binned experimental length distributions for joined A tubes and C tubes are shown in Figures 6 and 7.

In isolation, nanotube length does not change over the incubation period where joining was studied. We first tested whether nanotube dynamics within the time regime covered by our study are controlled purely by end-to-end joining or whether changes in length also resulted from nucleation, growth or melting. To characterize how much growth and melting would be expected to occur in the absence of the potential for joining, we measured how the lengths of seeded B-type nanotubes, which cannot join with themselves, changed

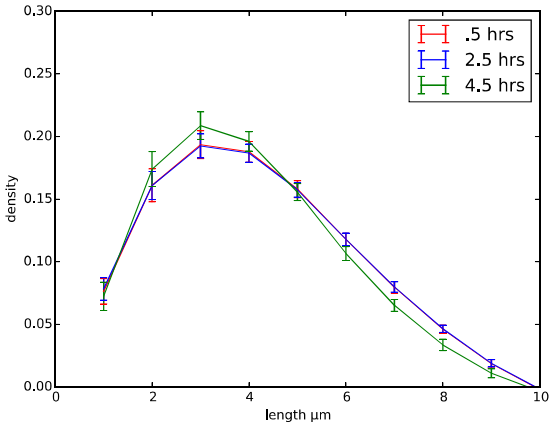

Figure 5. Length distributions of B-type majority species nanotubes at each time point. Error bars represent the standard error of the mean, calculated using bootstrapping with 1000 replicates.

over time. Seeded B-type nanotubes were prepared as described in Methods; however, instead of combining the A-type and B-type nanotubes in a 1:5 ratio after 15 hours, the B-type nanotubes were imaged separately. B-type nanotube lengths were then measured at .5 hrs, 2.5 hrs, and 4.5 hrs (Figure 4). As shown in Figure 4, the mean lengths of B-type nanotubes did not change significantly over the incubation period where joining was studied, suggesting that the net rate of nanotube growth and melting was no more than ~.1µm/hr. Note that only seeded nanotubes were considered here. We conclude that growth (or melting) processes do not contribute significantly to nanotube dynamics under the conditions of our study and may safely be disregarded in our models of end-to-end joining.

The length distribution of the unjoined excess nanotube species does not change over time as a result of end-to-end joining. Our goal in combining the A and B species in a 1:5 ratio was to ensure that the length distribution of the excess species (species B) was not affected by end-to-end joining with the minority species (species A). To test whether this goal was achieved we measured the length distributions of the unjoined species B (excess) at each time point (Figure 5). As shown in Figure 5, any changes in the unjoined excess nanotube length distributions over time are within experimental error established by bootstrapping. This indicates that end-to-end joining does not significantly affect the length distribution of the B nanotubes over time. Given that length distribution and concentration of species B nanotubes do not change over time, we expect the joining rate for a given A nanotube should be roughly constant over time, which simplified the interpretation of our results. That is, the length dependence of joining can be observed by observing changes in the length distribution of A nanotubes in the presence of B nanotubes.

Generating simulated length distributions for the three models using a given rate parameter. To determine whether a model accurately captured the joining rates for a range of nanotube lengths, we simulated the joining process using each model and compared the results of the simulation at different times to our experimental measurements. To facilitate this comparison, experimentally measured lengths were binned in an identical fashion to the simulated lengths (using the fit to rate parameters as described below) so that their histograms may be overlaid (Figures 6,7). Using the fact that nanotubes did not appear to grow or shrink over time, the length distributions of unjoined A-type and B-type nanotubes at time 0 hrs (initial conditions) were generated by assigning the A-type and B-type nanotubes from the first time point (.5 hrs) an unjoined status.

Designing the cost function. To assess the accuracy of each model we chose a cost function that requires a model to predict both the mean joining rate and length-dependent variations in the rate at each time point where experimental data was collected:

Equation 3

$$E_{total}{}^2 = (E_{joining\_fraction}{}^2) + (E_{joined\_Atube\_CDF}{}^2) + (E_{Ctube\_CDF}{}^2)$$

Our cost function thus simply adds the difference between experimental and simulated values of three attributes at each time point: (1) error in a model's prediction of the fraction of total A tubes that are joined ($E_{joining}$), (2) error in a model's prediction of the cumulative length distribution function of the lengths of the A-tube component of C-type nanotubes ($E_{joined\_Atube\_CDF}$), (3) error in a model's prediction of the cumulative length distribution function for C-type nanotubes (E_{Ctube_CDF}). Both the cumulative distribution function (CDF) of the lengths of the A type domains within the C tubes and the C tube CDF contain information on the length dependence of end-to-end joining. The CDF of A tube domains within C tubes effectively measures the likelihood that an A tube of a particular length is not joined to a B tube of any length. Meanwhile, the C tube CDF measures the likelihood of two tubes of a particular total length (A length + B length = C length) joining and therefore provides additional information on length-dependence. In our study, each error term is given equal weighting; as we will later demonstrate, differently weighting these terms would not effect our conclusions. Our error function measures differences in fractions of nanotube populations at each bin and is therefore dimensionless.

Optimal parameters for each model. Each model of the end-to-end joining rate has one fitted parameter. In the constant model, the fitted parameter is simply the bimolecular rate constant $\boldsymbol{\beta}$ (in /M/s). In the Hill and Hariadi models the fitted parameters are the prefactors $\boldsymbol{A_{Hill}}$ (/M/s) and $\boldsymbol{A_{Hariadi}}$ (/M/s), respectively, (see equations 1 and 2) that precede the particular (dimensionless) length-dependent term in the joining rate equations. The lengths used in both the Hill and Hariadi models are made dimensionless by dividing by the nanotube diameter (approximated as .015 µm for seeded nanotubes).[29] We used a brute force parameter scan to identify optimal values, and the associated cost function errors, for each fitted parameter in each model. In all three cases, the optimal parameter value represents a distinct minimum in the cost

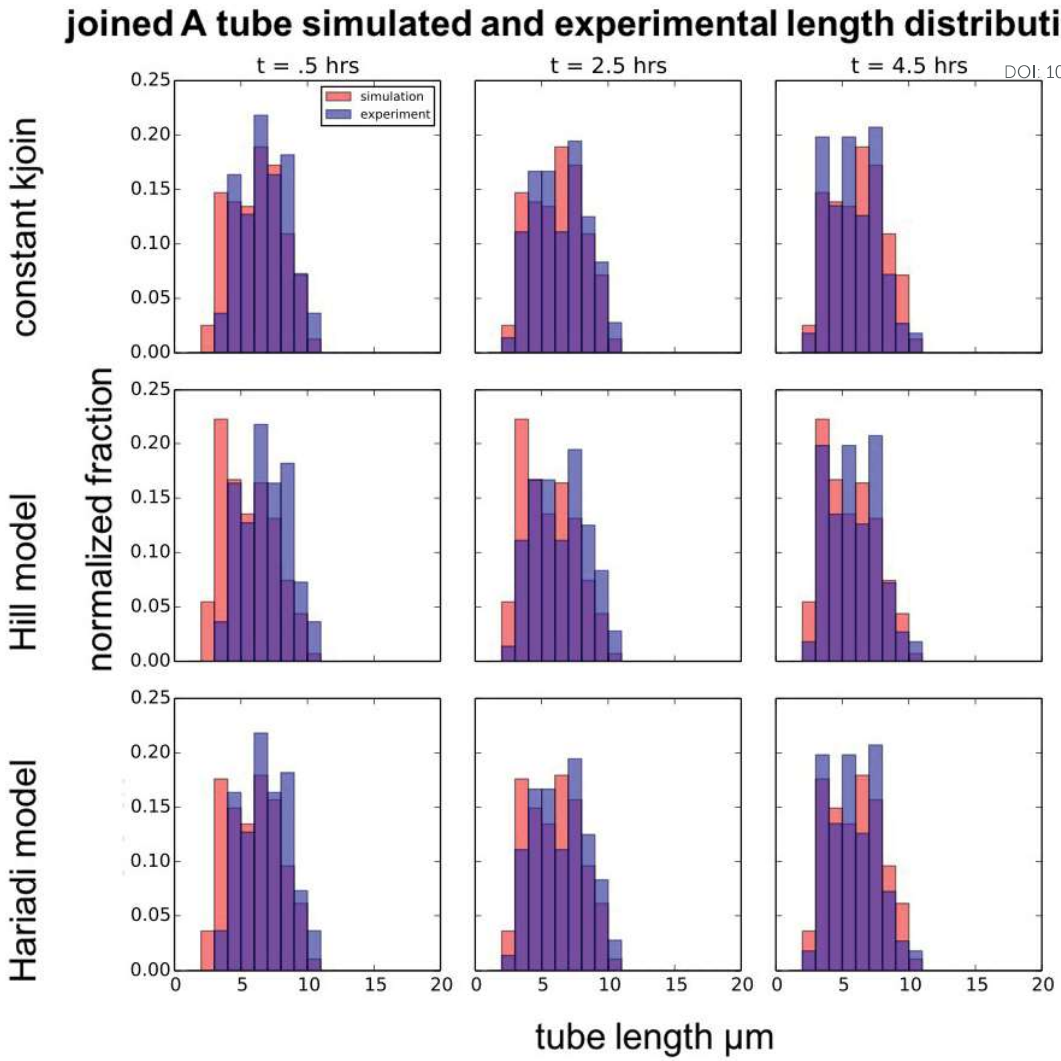

Figure 6. Experimental (blue) and simulated (red) length distributions for joined A-type nanotubes.

function. The optimal parameter values and the corresponding cost function errors found for each model are shown in Table 1.

The optimal parameter values identified by all three models are consistent with prior measurements. For the constant model, the ~4e6 /M/s rate constant that was fit to the data is consistent with prior measurements of the reaction rate for nanotube tile attachment,[29] nanotube joining rates made with assumption that the joining rate is length independent,[32] and the hybridization rates of DNA origami[51]. In both the Hill and Hariadi models, the optimal prefactor must be multiplied by an appropriate (dimensionless) length-dependent term to yield a joining rate in /M/s for nanotube reactants of particular lengths. The distribution of lengths of unjoined nanotubes measured in our experiments are centered around 5 μm, so, to compare the fits for the Hill and Hariadi models to previous rate measurements, we consider the joining of two 5 μm nanotubes. Using the Hill model with the optimal prefactor yields a joining rate of ~2e6 /M/s and using the Hariadi model with the optimal prefactor yields a joining rate of ~3e6 /M/s. Confidence intervals on the optimal parameter values were computed using bootstrapping, with 1000 replicates each, randomly selecting 50% of the experimental data and then performing a brute force scan to identify an optimal parameter based on a random subset of the data. These results suggest that using our data, we can estimate the rate constants within a factor of 2-3.

All three models show agreement with experimental data, with the constant and Hariadi models marginally outperforming Hill. Using the optimal parameters calculated for each joining model, we generated simulated nanotube length distributions for the A domains of joined nanotubes, unjoined A nanotubes, and C nanotubes at each experimentally measured time point. The normalized simulation distributions predicted by each model are compared with normalized experimentally measured length distributions in Figures 6 and 7. In general, both the Hariadi and constant joining models overlap well with the experimental data, with the Hill joining model showing weaker agreement, particularly when comparing the C tube length distributions and comparing data

View Article Online
DOI: 10.1039/C9ME00068B

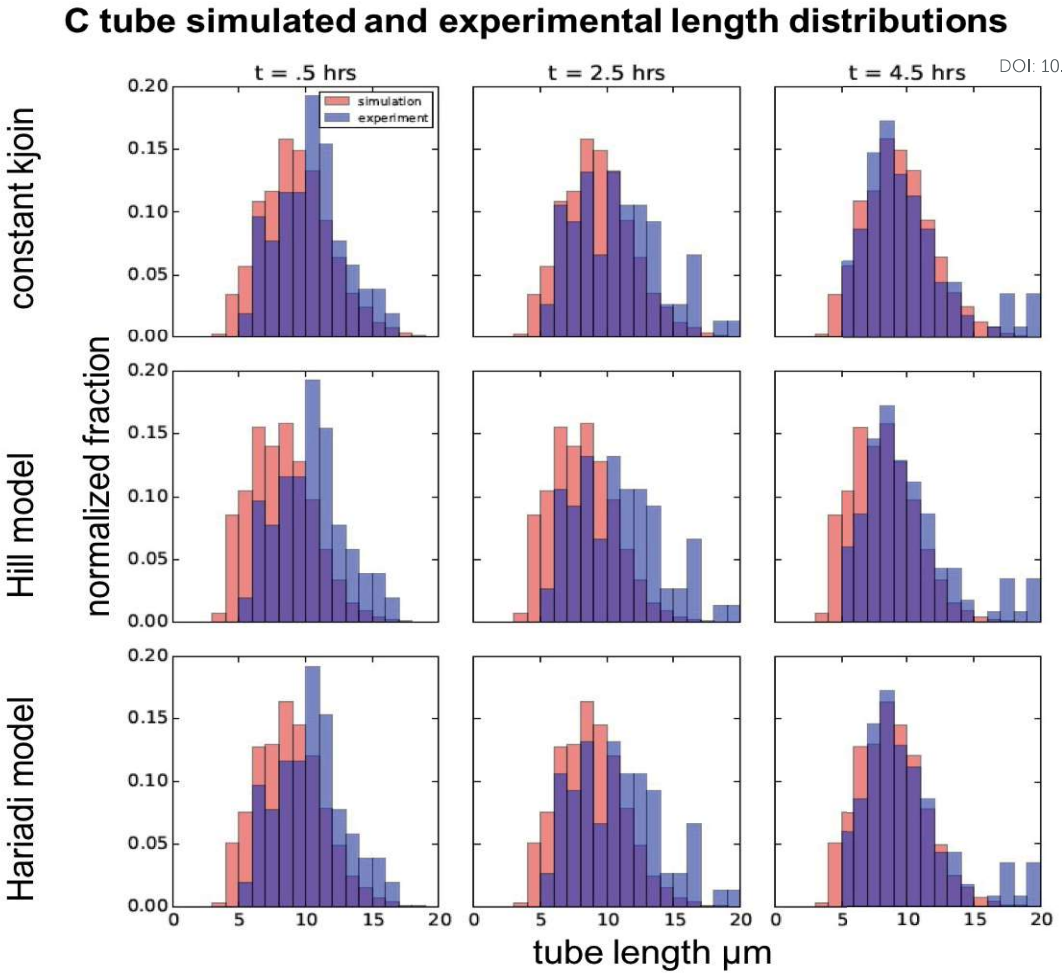

Figure 7. Experimental (blue) and simulated (red) length distributions for C-type nanotubes.

at the earliest time point. This observation is also in agreement with the tabulated cost function, or error, values in Table 1, which indicate that the constant model has the lowest error, followed by Hariadi and then Hill. (Note that error values are dimensionless). Additionally, the data in Table 1 shows that the difference in error between the constant and Hill models is nearly three times as large as the difference in error between the constant and Hariadi models.

The constant joining rate and Hariadi models outperform Hill with statistical significance. To evaluate the statistical significance of our cost function ranking (constant < Hariadi < Hill) we computed confidence intervals on the cost function error. Confidence intervals on the cost function error associated with the optimal parameter value were computed using the same bootstrapping procedure used for the optimal parameter confidence intervals; however, for each replicate the error was calculated using the optimal parameter identified using the full data set. Optimal parameter values and associated errors, as well as 90% confidence intervals for both parameter values and associated errors are shown in Table 1. As seen in Table 1, the 90% confidence interval on the constant model error overlaps with interval for Hariadi. Likewise, the confidence interval for the Hariadi model overlaps with the Hill model. This is supported by the fact that a visual distinction between the constant and Hariadi models in Figures 6 and 7 is more difficult to make than a distinction between the constant and Hill models. Using our bootstrapping results for the cost function error we calculate that the probability of observing a rank order of constant model < Hariadi model is ~92.4%, a rank order of constant model < Hill model is ~99.9%, and a rank order of Hariadi model < Hill model is ~98.3%. The constant and Hariadi models outperform Hill; however, a distinction between the constant and Hariadi models is more difficult to make.

Joining rates predicted by fits to the Hill and Hariadi joining models differ just 3-10 fold over the range of tube lengths in our experiments. When considering joining between two 5 μm nanotubes, the rates predicted by both the Hill and Hariadi models are similar. However, the length-dependent scaling of each model differs over the range of lengths considered in our experiments. For example, let us compare the difference in predicted joining rates for a 5 μm tube joining with a 1 μm tube (faster) vs a 5 μm tube joining with a 10 μm tube (slower) using both the Hill and Hariadi models. In the Hill model, the rate of joining with the 10 μm tube is approximately seven times slower than the rate of joining with the 1 μm tube. However, in the Hariadi model, joining with the 10 μm tube is only three times

slower than joining with the 1 μm tube. The computed rate constants for these "long tube" and "short tube" joining reactions using both models are shown in Table 1. While the range of joining rates (3 – 10 fold) is not dramatic, we do expect, given our distribution of tube lengths, that there should be a detectable difference in the joining rate in our experiments. However, no such length-dependence is detected, suggesting that the constant rate joining model is the most accurate.

The relative ranking of the models is not influenced by the way nanotube lengths were binned. Our cost function measures differences between the fraction of nanotubes in a particular range of lengths, a bin, at particular times measured in experiments and predicted by a particular model. To ensure that our ranking of the three end-to-end joining models is robust to how the lengths were binned, we repeated our fitting protocol using bin widths of .9 μm and 1.1 μm (still capping the maximum tube length at 20 μm). The relative ranking of the three end-to-end joining models, as well as the size of the confidence intervals, was unaffected by the new bin widths.

The relative ranking of the models is not influenced by the form of the cost function. Our cost function compares a linear combination of the error between experimental and simulated values of: (1) the fraction of joined nanotubes, (2) the cumulative length distribution function of the A-type domains of joined nanotubes, and (3) the cumulative length distribution function for C-type nanotubes. In our cost function, these errors were summed without being weighted. To ensure that our predictions are not strongly dependent on how each term of the cost function was weighted, we repeated our fitting protocol with three different cost functions: a cost function with only the joining fraction term active, a cost function with only the joined A-type cumulative distribution term active, and a cost function with only the C-type cumulative distribution term active. Plots of the fitted parameter vs. the error for each of the three joining models (constant, Hill, and Hariadi) using each of the three cost functions are shown in Figure 8. The optimal parameters achieved using each of these cost functions are within a factor of two of the optimal parameters achieved using the cost function in Equation 3 (Figure 8, leftmost column), except that for the constant joining rate model, the cumulative distribution function cost functions give a constant error for all possible reaction rates as expected.

Further, each optimum lies in a deep local minimum for the error: that is, the error increases nonlinearly as the parameter is increased or decreased from the optimum value. For the joining fraction cost function in particular, one can see why this scaling of the error is similar for all three models. For both models where joining rates are length-dependent, shorter tubes join faster and longer tubes join slower; averaging the joining rate over the symmetric distribution of tube lengths in our experiments cancel out these effects to produce a net joining fraction similar to a mean joining rate that is independent of nanotube length.

The reason the models do not all fit the data equally well is because some models predict the shapes of the cumulative length distributions of the A-type domains of the C nanotubes and C-type nanotubes at different times more poorly than others do (Figure 8, center and rightmost columns). In the constant model, the error terms in the cost function corresponding to these length distributions have no dependence on the joining rate constant (Figure 8, top center and top right plots) because all nanotubes join at the same rate. Thus, the shapes of the normalized cumulative length distribution functions cannot change for any joining rate. For the Hariadi and Hill models, there is significant dependence of the error on both the joined A-type and C-type cumulative length distribution terms (Figure 8, four plots in lower right corner). There are two significant features in these plots: (1) the global trend of error decreasing with increasing parameter value, and (2) the existence of a local minimum at intermediate parameter values. The global trend can be rationalized for the cumulative distribution of the lengths of the of joined nanotubes by considering what should happen to the error when the joining rate prefactor is very large. Here, end-to-end joining occurs so quickly that, regardless of nanotube length, by the first time point almost 100% of nanotubes should be joined. In this case, the distribution of the lengths of A-type joined tubes should be exactly the same as the initial distribution of A-type unjoined tubes, giving roughly the same error for this term as for the constant joining rate model for a sufficiently large rate. By contrast, at very low joining rates, only the shortest nanotubes should join with any frequency, leading to length distributions of joined A-type nanotubes containing only short nanotubes. Since very little dependence on length was observed, the predicted distribution would be very different than the observed one, leading to a large error. The error in predicting the length of A-domains of the C-type nanotubes should follow the same trends, so that this general trend of decreasing error would also be seen for this component of the cost function. Thus, the trend toward lower error at higher parameter values implies that the constant model is the most appropriate given the experimental data. The local minima in these plots represent intermediate parameter ranges where optimal fits can be found; however, they do not represent the true global minimum error for the model.

View Article Online
DOI: 10.1039/C9ME00068B

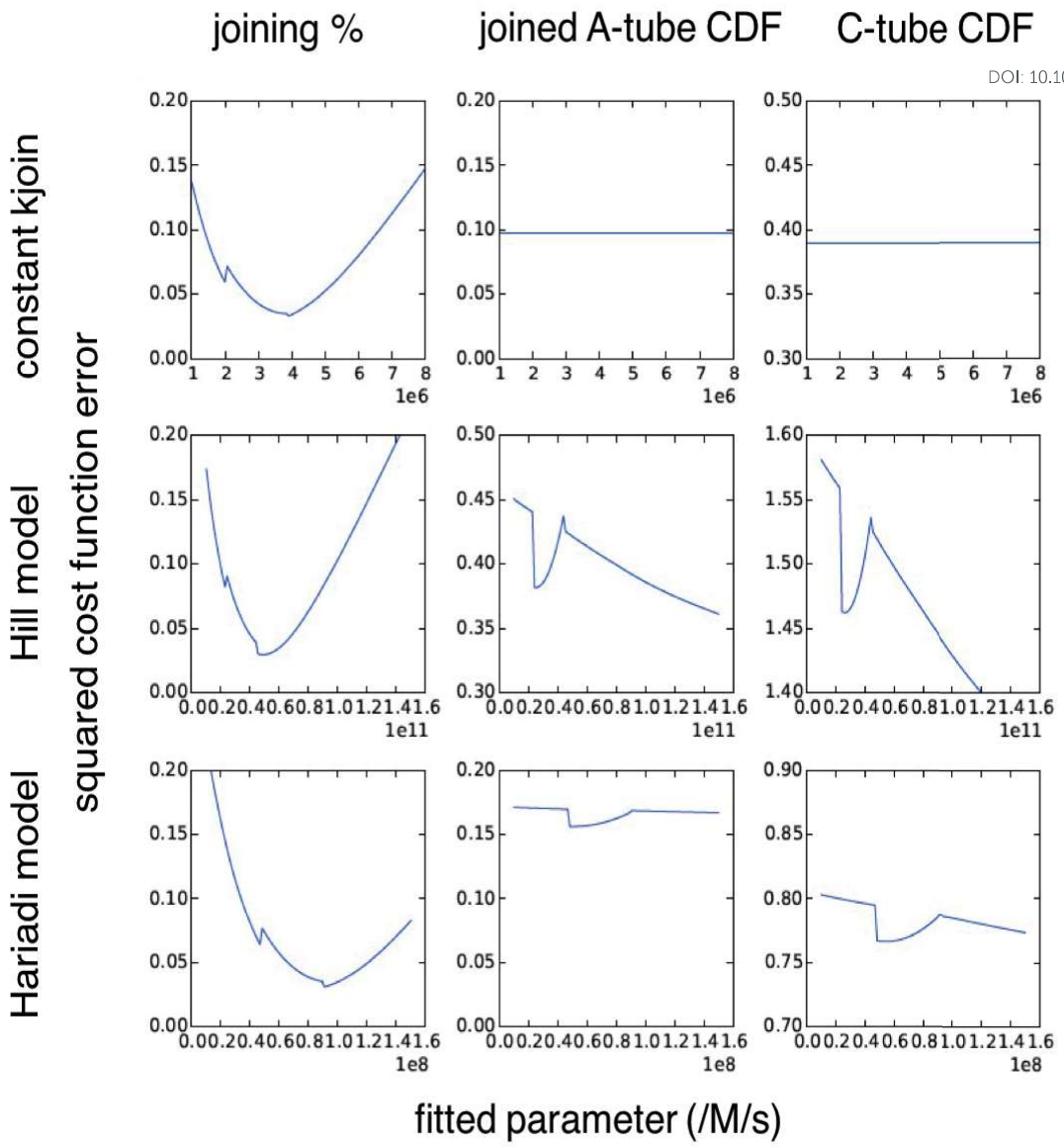

Figure 8. Comparison of three cost function components (joining %, joined A-tube CDF, C-tube CDF) for each of the three joining models (constant k_{join}, Hill model, Hariadi model).

For all three models a similar error is achieved using only the joining fraction as the cost function. Moving away from this minimum error, the error rises nonlinearly with deviations in parameter (Figure 8, leftmost column). Using the constant model, neither of the cumulative distribution terms have any dependence on parameter value (they merely add a constant error). Thus, the optimal parameter for the constant model is determined purely by the joining fraction term. In contrast, for the cumulative distribution terms in both the Hill and Hariadi models, the global trend toward lower error with higher parameter values is linear and is cancelled out by the nonlinear increase in error from the joining fraction term. This cancellation of a term that scales linearly by a term that scales nonlinearly is independent of the particular weights on each term in the linear combination and restricts the available parameter space available to the Hill and Hariadi models. That is, for a given cost function, fitting the Hill and Hariadi model leads to a trade-off. Fitting the right overall joining fraction leads to a too-large shift in the cumulative distribution functions with time, while fitting the cumulative distribution functions over time leads to a too-small average joining rate. This compromise again supports the length-independent joining rate for use in understanding DNA nanotube joining as both the simplest model and the model that best explains our observations.

Conclusions

In this study, we experimentally characterized the length-dependence of the end-to-end joining rate of DNA nanotubes by measuring the lengths of nanotubes before and after joining at different times during the joining process. We then tested the ability of three different models for the end-to-end joining rate (constant rate, Hill, and Hariadi) to reproduce the experimental length data using an ODE model of nanotube joining. All three joining models predict physically realistic average joining rates

model	fitted parameter (/M/s)	.90 CI parameter (/M/s)	cost function	.90 CI cost function	predicted kjoin for long tubes (/M/s)	predicted kjoin for short tubes (/M/s)
constant	3.86E+06	3.78E+06 - 3.91E+06	0.521	0.322 -0 .962	3.86E+06	3.86E+06
Hariadi	7.18E+07	6.66E+07 - 7.76E+07	0.974	0.618 - 1.61	1.95E+06	5.77E+06
Hill	2.98E+10	2.31E+10 - 3.76E+10	1.92	1.31 - 2.87	8.09E+05	5.98E+06

Table 1. Compiled data on parameter fits and corresponding error. Confidence intervals were generated using bootstrapping with 1000 replicates. "Min" joining rates are calculated for a 5 µm tube joining to a 10 µm tube, "max" joining rates are calculated for a 5 µm tube joining to a 1 µm tube.

that are consistent with prior measurements.[29, 51, 52] We ranked each of the three joining models using a cost function that compares both mean joining rate and length-dependence of joining rate between each model and experiment. Using this cost function, the constant model is ranked the most accurate, followed by the Hariadi model and lastly the Hill model. Confidence intervals on the cost function error and the ranking probabilities (a rank order of constant < Hariadi is ~92.4%, constant < Hill is ~99.9%, and Hariadi < Hill is ~98.3%) suggest that the constant and Hariadi models significantly outperform Hill; however, a distinction between the constant and Hariadi models is less certain. Overall, all three joining models provide an acceptable fit to the experimental data when simulated and experimental histograms are overlaid.

One possible reason the differences between the models were so small is that the differences in the joining rates between nanotubes of the lengths we studied is not expected to be that large for the Hariadi and Hill models. We measured joining rates for nanotubes with lengths centered around 5 µm and vary between 1 and 10 µm (Figures 6 and 7). As shown in Table 1, the expected variation in joining rate over this range is approximately three-fold for the Hariadi model and seven-fold for the Hill model. These variations in joining rate are significant and produce a higher error in the Hariadi and Hill models relative to the constant rate model, particularly so for the Hill model. However, in a study that included nanotubes with a wider range of lengths, the Hill and Hariadi models would predict a larger range of joining rates. In such a study, the differences between the three joining rate models would be exacerbated and more easily detected by our analysis.

DNA nanotubes provide an ideal model system for the measurement of polymer end-to-end joining rates. However, it is unclear how well our results translate to joining processes that do not occur because of Watson-Crick hybridization. The length-independent joining that we observe in this study disagrees with prior results on microtubules,[36-39] amyloid fibrils,[40-42] and actin filaments,[43, 44] all of which obey the length-dependent model prescribed by Hill. Our length-independent joining rates suggest that translational and rotational diffusion of DNA nanotubes is not the rate-limiting step in end-to-end joining.

The question of length-dependent nanotube joining is a special case of a more general question: How does the size of a DNA nanostructure determine how fast it hybridizes with others? It appears there is no systematic answer to this question and that the answer may depend on the length scale involved. For instance, Zenk *et al.*[51] observed that dimerization rate constants for 60 nm scaffolded DNA origami nanostructures are of the same order of magnitude as rate constants for bimolecular association of small, complementary DNA strands. Jiang *et al.*[52] observed that the second-order rate constant of DAE-E DNA tile homodimer formation is two-fold higher than the rate constant for single stranded DNA hybridization, despite the fact than DNA tiles are bulkier than single stranded DNA oligos. Jiang *et al* also found that tile rigidity strongly affects the second-order rate constant despite having no impact on translational or rotational diffusion. A range of measurements of DNA hybridization from 20-bp oligos,[53, 54] to DNA double-crossover tiles,[52] to tiles hybridizing to larger nanostructures all predict somewhat similar rate constants for similar salt-conditions. Our study further shows that two micron-scale structures again join at a similar rate. These results together suggest that DNA hybridization is not a diffusion-limited process under these conditions.

Better understanding of what controls these rates will be critical for the kinetic control of DNA self-assembly. Factors that do affect the rates of DNA nanostructure binding include multivalency, *i.e.* the existence of multiple single-stranded binding sites that can hybridize on each of the reactions and the rigidity of the reactants,[55] although none of these affect rates more than a factor of 3-5. Temperature[54, 56, 57] and salt composition[50, 58, 59] also affect rates, although the dependence on temperature does not obey the Arrehenius rate law.[57] However, one potential advantage of the similarity of DNA nanostructure hybridization rates across such a wide range of reactant size scales is that we can reasonably assume a single rate of interaction between many different DNA nanostructures. In combination with the ability to predict the free-energy of association,[50] this fact should allow us to design relatively accurate models of the kinetics of DNA self-assembly processes without the need to measure the thermodynamics and kinetics of association for each potential component or intermediate.

Acknowledgements

This research was supported by DOE grant SC-0010595 for support of all personnel and experiments, analysis and manuscript preparation. Computational resources were provided by the Maryland Advanced Research Computing Center. We wish to acknowledge Dr. Joshua Fern and Samuel Schaffter for helpful discussions and feedback on the manuscript.

Notes and references

DNA sequences

DNA sequences and cadnano schematics for DNA origami seed staples, DNA origami seed adapters, and DNA tiles are included in the supplemental file "sequences.pdf"

‡ Footnotes relating to the main text should appear here. These might include comments relevant to but not central to the matter under discussion, limited experimental and spectral data, and crystallographic data.

§

§§

etc.

1. K. E. Drexler, *Engines of Creation*, Fourth Estate, 1986.
2. R. D. Barish, R. Schulman, P. W. K. Rothemund and E. Winfree, *P Natl Acad Sci USA*, 2009, **106**, 6054-6059.
3. S. M. Douglas, H. Dietz, T. Liedl, B. Hogberg, F. Graf and W. M. Shih, *Nature*, 2009, **459**, 414-418.
4. B. Wei, M. J. Dai and P. Yin, *Nature*, 2012, **485**, 623-+.
5. M. D. Hager, P. Greil, C. Leyens, S. van der Zwaag and U. S. Schubert, *Adv Mater*, 2010, **22**, 5424-5430.
6. L. N. Green, A. Amodio, H. K. K. Subramanian, F. Ricci and E. Franco, *Nano Lett*, 2017, **17**, 7283-7288.
7. D. Han, S. Pal, Y. Liu and H. Yan, *Nat Nanotechnol*, 2010, **5**, 712-717.
8. T. Gerling, K. F. Wagenbauer, A. M. Neuner and H. Dietz, *Science*, 2015, **347**, 1446-1452.
9. F. Zhang, J. Nangreave, Y. Liu and H. Yan, *Nano Lett*, 2012, **12**, 3290-3295.
10. M. Siavashpouri, C. H. Wachauf, M. J. Zakhary, F. Praetorius, H. Dietz and Z. Dogic, *Nat Mater*, 2017, **16**, 849-856.
11. G. Tikhomirov, P. Petersen and L. Qian, *Nat Nanotechnol*, 2017, **12**, 251-259.
12. J. Zheng, J. J. Birktoft, Y. Chen, T. Wang, R. Sha, P. E. Constantinou, S. L. Ginell, C. Mao and N. C. Seeman, *Nature*, 2009, **461**, 74-77.
13. F. Zhang and H. Yan, *Nature*, 2017, **552**, 34-35.
14. L. L. Ong, N. Hanikel, O. K. Yaghi, C. Grun, M. T. Strauss, P. Bron, J. Lai-Kee-Him, F. Schueder, B. Wang, P. Wang, J. Y. Kishi, C. Myhrvold, A. Zhu, R. Jungmann, G. Bellot, Y. Ke and P. Yin, *Nature*, 2017, **552**, 72-77.
15. K. F. Wagenbauer, C. Sigl and H. Dietz, *Nature*, 2017, **552**, 78-83.
16. G. Tikhomirov, P. Petersen and L. Qian, *Nature*, 2017, **552**, 67-71.
17. F. Praetorius, B. Kick, K. L. Behler, M. N. Honemann, D. Weuster-Botz and H. Dietz, *Nature*, 2017, **552**, 84-87.
18. A. M. Mohammed, P. Sulc, J. Zenk and R. Schulman, *Nat Nanotechnol*, 2017, **12**, 312-316.
19. P. W. Rothemund, N. Papadakis and E. Winfree, *PLoS Biol*, 2004, **2**, e424.
20. A. J. Turberfield, *Nat Chem*, 2011, **3**, 580-581.
21. X. Wei, J. Nangreave and Y. Liu, *Acc Chem Res*, 2014, **47**, 1861-1870.
22. P. W. Rothemund, *Nature*, 2006, **440**, 297-302.
23. K. E. Dunn, F. Dannenberg, T. E. Ouldridge, M. Kwiatkowska, A. J. Turberfield and J. Bath, *Nature*, 2015, **525**, 82-86.
24. S. Jiang, F. Hong, H. Hu, H. Yan and Y. Liu, *Acs Nano*, 2017, **11**, 9370-9381.
25. J. Valero, F. Lohmann, D. Keppner and M. Famulok, *Chembiochem*, 2016, **17**, 1146-1149.
26. W. Li, Y. Yang, S. Jiang, H. Yan and Y. Liu, *J Am Chem Soc*, 2014, **136**, 3724-3727.
27. S. Woo and P. W. Rothemund, *Nat Commun*, 2014, **5**, 4889.
28. J. J. De Yoreo, P. U. Gilbert, N. A. Sommerdijk, R. L. Penn, S. Whitelam, D. Joester, H. Zhang, J. D. Rimer, A. Navrotsky, J. F. Banfield, A. F. Wallace, F. M. Michel, F. C. Meldrum, H. Colfen and P. M. Dove, *Science*, 2015, **349**, aaa6760.
29. A. M. Mohammed and R. Schulman, *Nano Lett*, 2013, **13**, 4006-4013.
30. P. Petersen, G. Tikhomirov and L. Qian, *Nat Commun*, 2018, **9**, 5362.
31. A. Ekani-Nkodo, A. Kumar and D. K. Fygenson, *Phys Rev Lett*, 2004, **93**.
32. R. F. Hariadi, E. Winfree and B. Yurke, *P Natl Acad Sci USA*, 2015, **112**, E6086-E6095.
33. P. W. K. Rothemund, A. Ekani-Nkodo, N. Papadakis, A. Kumar, D. K. Fygenson and E. Winfree, *J Am Chem Soc*, 2004, **126**, 16344-16352.
34. T. L. Hill, *Biophys J*, 1983, **44**, 285-288.
35. J. Riseman and J. G. Kirkwood, *J Chem Phys*, 1950, **18**, 512-516.
36. M. Bachand, N. F. Bouxsein, S. Cheng, S. J. von Hoyningen-Huene, M. J. Stevens and G. D. Bachand, *Rsc Adv*, 2014, **4**, 54641-54649.
37. A. C. Greene, M. Bachand, A. Gomez, M. J. Stevens and G. D. Bachand, *Chem Commun (Camb)*, 2017, **53**, 4493-4496.
38. R. C. Williams and L. A. Rone, *Protoplasma*, 1988, **145**, 200-203.
39. R. C. Williams, Jr. and L. A. Rone, *J Biol Chem*, 1989, **264**, 1663-1670.
40. J. D. Harper, S. S. Wong, C. M. Lieber and P. T. Lansbury, Jr., *Biochemistry*, 1999, **38**, 8972-8980.
41. R. M. Murphy and M. M. Pallitto, *J Struct Biol*, 2000, **130**, 109-122.
42. S. J. Tomski and R. M. Murphy, *Arch Biochem Biophys*, 1992, **294**, 630-638.
43. A. Teubner and A. Wegner, *Bba-Protein Struct M*, 1996, **1297**, 214-218.
44. D. B. Murphy, R. O. Gray, W. A. Grasser and T. D. Pollard, *J Cell Biol*, 1988, **106**, 1947-1954.
45. D. K. Agrawal, R. Jiang, S. Reinhart, A. M. Mohammed, T. D. Jorgenson and R. Schulman, *Acs Nano*, 2017, **11**, 9770-9779.
46. S. van der Walt, J. L. Schonberger, J. Nunez-Iglesias, F. Boulogne, J. D. Warner, N. Yager, E. Gouillart, T. Yu and c. scikit-image, *PeerJ*, 2014, **2**, e453.
47. J. Canny, *IEEE Trans Pattern Anal Mach Intell*, 1986, **8**, 679-698.
48. T. Y. Zhang and C. Y. Suen, *Commun. ACM*, 1984, **27**, 236-239.
49. K. C. Y. V. Mardanlou, L.N. Green, R.F. Subramanian, J. Kim, E. Franco, *Natural Computing*, 2017, **17**.
50. J. SantaLucia, Jr. and D. Hicks, *Annu Rev Biophys Biomol Struct*, 2004, **33**, 415-440.
51. J. Zenk, C. Tuntivate and R. Schulman, *J Am Chem Soc*, 2016, **138**, 3346-3354.
52. S. X. Jiang, H. Yan and Y. Liu, *Acs Nano*, 2014, **8**, 5826-5832.
53. Y. Gao, L. K. Wolf and R. M. Georgiadis, *Nucleic Acids Res*, 2006, **34**, 3370-3377.
54. L. E. Morrison and L. M. Stols, *Biochemistry*, 1993, **32**, 3095-3104.
55. J. Nangreave, H. Yan and Y. Liu, *Biophys J*, 2009, **97**, 563-571.
56. M. E. Craig, D. M. Crothers and P. Doty, *J Mol Biol*, 1971, **62**, 383-401.
57. C. Chen, W. Wang, Z. Wang, F. Wei and X. S. Zhao, *Nucleic Acids Res*, 2007, **35**, 2875-2884.
58. A. Bosco, J. Camunas-Soler and F. Ritort, *Nucleic Acids Res*, 2014, **42**, 2064-2074.
59. M. E. Polinkovsky, Y. Gambin, P. R. Banerjee, M. J. Erickstad, A. Groisman and A. A. Deniz, *Nat Commun*, 2014, **5**, 5737.

View Article Online
DOI: 10.1039/C9ME00068B